Supplementary Information

Two-dimensional Reconfigurable Photodiode for In-Sensor Color Filtering and Spectral Logic

Xiaokun Guo[1], Yaoqiang Zhou[2,*], Yufeng Zhang[3], Xinyi Zhao[1], Yue Pang[1], Lei Tong[1], Zhipei Sun[3,*], Jianbin Xu[1,*]

1, Department of Electronic Engineering and Materials Science and Technology Research Center, The Chinese University of Hong Kong, Hong Kong SAR, China

2, Department of Optical Physics, Beijing Institute of Technology, China

3, Department of Electronics and Nanoengineering, Aalto University, Finland

*Corresponding author: yaoqiang.zhou@bit.edu.cn; zhipei.sun@aalto.fi; jbxu@ee.cuhk.edu.hk

Supplementary Note 1. Aggregation-selected and pattern growth of PTCDI-C_{13}

To realize spatially defined doping in WSe_2 homojunctions, we developed a substrate-engineered, aggregation-selective growth strategy for PTCDI-C_{13}. This organic semiconductor forms two distinct aggregation types—*J*-aggregates and *H*-aggregates—depending on its molecular arrangement configuration (**Supplementary Figure 1a**). *J*-aggregates exhibit strong exciton coupling between adjacent molecules, resulting in narrow-band absorption, while *H*-aggregates, with antiparallel dipole alignments and weaker exciton coupling, display broader absorption profiles due to repulsive excitonic interactions.

Owing to van der Waals heteroepitaxy, PTCDI-C_{13} preferentially assembles into *J*-aggregates on hexagonal boron nitride (hBN), while *H*-aggregates form on bare SiO_2. As shown in **Supplementary Figure 1b**， to spatially define these domains, few-layer hBN was first transferred onto a SiO_2/Si substrate and patterned via electron beam lithography (EBL), followed by reactive ion etching (RIE) using SF_6 and Ar gases. The one-step physical vapor transport (PVT) process was then employed to deposit PTCDI-C_{13}, yielding selectively patterned regions of *J*- and *H*-aggregates.

Optical microscopy images of hBN/ SiO_2 before and after PTCDI-C_{13} deposition (**Supplementary Figure 1c-d**) confirm the integrity of the hBN pattern with well-defined edges. Atomic force microscopy (AFM) (**Supplementary Figure 1e**) indicates an hBN thickness of 2.3 nm. Photoluminescence (PL) mapping identifies distinct emission features from the two aggregate types of PTCDI-C_{13}, with peaks

centered at ~550 nm for *J*-aggregates and ~630 nm for *H*-aggregates (**Supplementary Figure 1f**), corroborating their spatial and spectral separation.

To further characterize their optical behavior, temperature-dependent PL spectra were collected over a range of 83–293 K. For *J*-aggregates, decreasing temperature suppresses thermal disorder and promotes larger aggregate domains, leading to a marked increase in emission intensity at 551.5 nm (**Supplementary Figure 1g**). *H*-aggregates show similar behavior, with increased intensity and a narrower emission bandwidth upon cooling (**Supplementary Figure 1h**).

The recombination dynamics of photoexcited carriers were further probed via time-resolved photoluminescence (TRPL) spectroscopy (**Supplementary Figure 1i**). *J*-aggregates exhibit a significantly shorter exciton lifetime of 0.53 ns compared to 1.88 ns in *H*-aggregates, indicating more efficient radiative recombination in the former due to enhanced excitonic coupling.

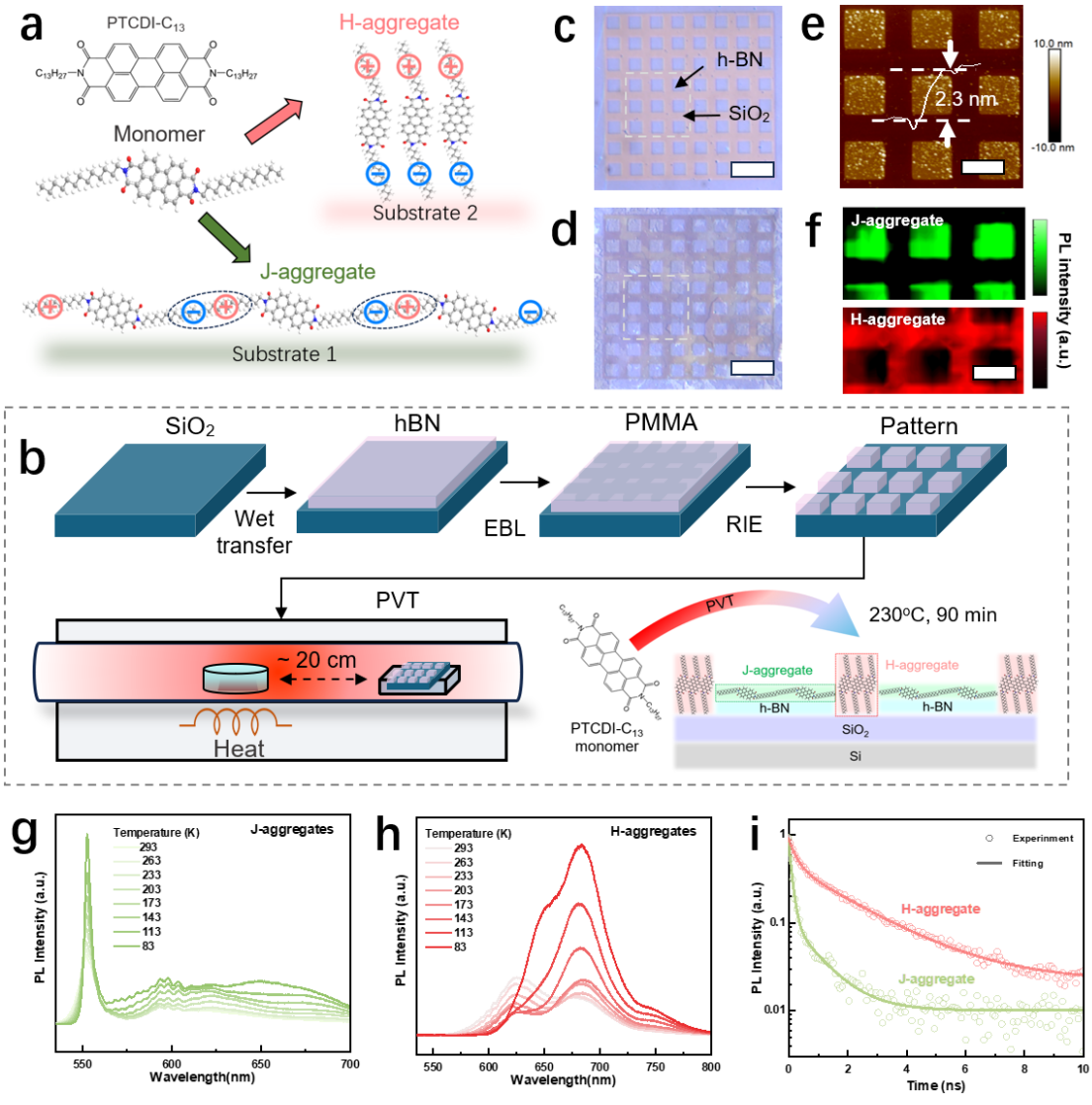

Supplementary Figure 1. **Aggregation-selected and pattern growth of PTCDI-C_{13}. (a)** Schematic molecular arrangement configuration of PTCDI-C_{13} in monomer, *J*- and *H*- aggregates. **(b)** Workflow diagram for aggregation-selected pattern growth of PTCDI-C_{13}. **(c)-(d)** Optical images of the patterned h-BN/SiO_2 substrate before **(c)** and after **(d)** depositing PTCDI-C_{13}. Scale bar: 20 μm. **(e)** AFM image of the h-BN/SiO_2 substrate. Scale bar: 5 μm. **(f)** PL mapping measured at emission wavelength of 550 nm and 630 nm indicating the distribution of *J*-aggregate and *H*-aggregate, respectively. Scale bar: 5 μm. **(g)-(h)** Low temperature PL spectra of *J*-aggregate **(g)** and *H*-aggregate **(h)** measured with a liquid N_2 cooling system. **(i)** TRPL spectra of the *J*-aggregate and *H*-aggregate. The fitting function of the bi-exponential decay is $R_t = A_1 exp(-t/\tau_1) + A_2 exp(-t/\tau_2)$. The average lifetime can be calculated using $\tau_{ave} = (A_1{\tau_1}^2 + A_2{\tau_2}^2)/(A_1\tau_1 + A_2\tau_2)$. The result shows that the τ_{ave} of the *J*-aggregate and *H*-aggregate is 0.53 ns and 1.88 ns, respectively.

Supplementary Note 2. Transconductance analysis

Here, we measured the transfer curves of the device after exposure to light pulses of 532 nm and 639 nm, both at an identical intensity of 1 mW/cm^2 and a duration of 5 seconds, as illustrated in **Supplementary Figure 2a-b**. The high resistance state (HRS) and low resistance state (LRS) were programmed using V_{GS} pulses of -15 V and 15 V, respectively. At V_{DS} = 1 V (**Supplementary Figure 2a**), the transfer threshold voltage (V_{th}) shifted rightward after exposure to the 532 nm (V_{th} = -2.24 V) and 639 nm (V_{th} = -1.84 V) lasers compared to the HRS (V_{th} = -2.89 V). Notably, the 639 nm illumination induced a larger V_{th} shift than the 532 nm light. In contrast, at V_{DS} = 2 V (**Supplementary Figure 2b**), the V_{th} after 532 nm illumination was about -0.69 V, which is higher than that observed with the 639 nm light (V_{th} = -1.16 V).

As shown in **Supplementary Figure 2c-d,** for clearer comparison, the transconductance (g_m) curves were calculated using:

$$g_m = \frac{\Delta I_{DS}}{\Delta V_{GS}}$$

Generally, a higher g_m value indicates more effective carrier transport across the junction barrier (Φ_{WSe2}). At a lower V_{DS} of 1 V (**Supplementary Figure 2c**), exposure to 639 nm illumination primarily leads to a photodoping effect in the *H*-WSe_2 region. In this case, hole transport within the valence band traverses a lower Φ_{WSe2} in the homojunction, resulting a higher g_m value that approaches the LRS. In contrast, 532

nm illumination photodopes either *H*-WSe_2 or *J*-WSe_2 region, leading to an enhanced Φ_{WSe2} in the homojunction due to the surface potential difference between *J*- and *H*- aggregates. This higher Φ_{WSe2} obstructs the hole transport across the junction region and causes a lower g_m value approaching the HRS. When the V_{DS} is increased to 2 V (**Supplementary Figure 2c**), both 639 nm and 532 nm illuminations enhance and rightward shift g_m, approaching the LRS. This is because the larger forward bias partially counteracts Φ_{WSe2}, facilitating hole transport and increasing g_m under both illumination conditions.

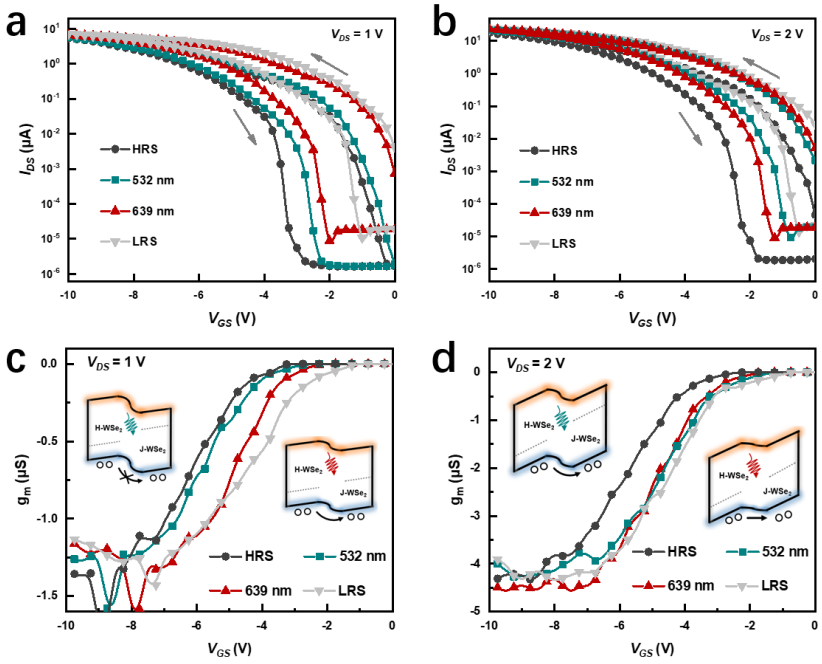

Supplementary Figure 2. **Transconductance analysis**. **(a)-(b)** Transfer curves following exposure to different light and electric pulses, with V_{GS} dual swept from 0 V to -10 V and back to 0 V at V_{DS} of 1 V **(a)** and 2 V **(b)**. **(c)-(d)** Extracted transconductance curves from the V_{GS} sweep ranging from 0 V to -10V at V_{DS} of 1 V **(c)** and 2 V **(d)**. The insets illustrate the evolution of the junction barrier (Φ_{WSe2}) under varying incident wavelengths and bias voltages.

Supplementary Note 3. Spectrally mixed dataset construction

To ensure that digit classification relies solely on spectral (color) information rather than intensity variations, we developed an iso-intensity RGB conversion protocol for the MNIST dataset.

First, all grayscale images were normalized to maintain identical total luminance (Σ I = constant). The dataset was then randomly divided into two groups for color encoding: Group A assigned mainly red

(R=1.0, G=0, B=0) to pixels with grayscale values >0.6 and mainly green (R=0, G=1.0, B=0) to pixels ≤0.6, while Group B adopted the inverse color scheme. Meanwhile, the blue channel was randomly incorporated as noise signal into the patterns. By strictly controlling the sum of RGB values to 1.0 for each pixel, we guaranteed identical intensity (I=R+G+B) across all pixels, ensuring spectral contrast was determined exclusively by hue (R/G ratio). Validation analysis confirmed all images shared identical intensity distributions (Σ I = 1.0 $\pm$ 0.01). This method effectively isolates spectral sensitivity as the sole variable in device testing, prevents intensity-based biases in the CNN classifier, and mimics real-world scenarios where encrypted information is carried by spectral signatures rather than brightness variations.

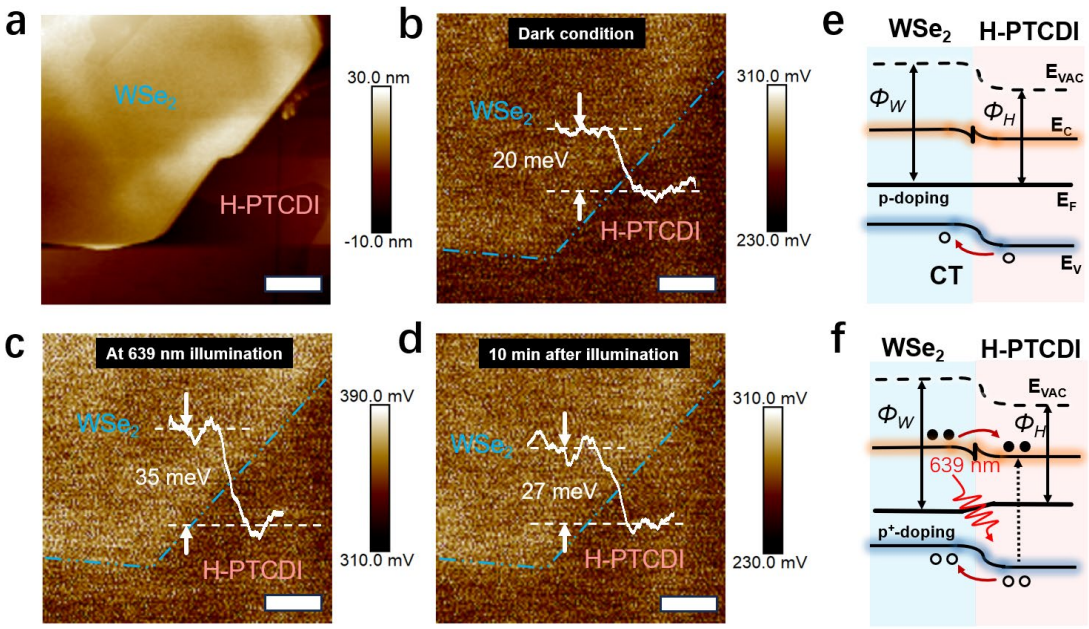

Supplementary Figure 3. Surface potential difference between WSe_2 and *H*-PTCDI measured by Kelvin probe force microscopy. **(a)** AFM image of WSe_2/*H*-PTCDI-C_{13} interface. Scale bar: 2 μm. **(b)-(d)** KPFM potential mappings of the WSe_2/*H*-PTCDI interface under various conditions: dark **(b)**, 639 nm illumination at 1 $mW \cdot cm^{-2}$ intensity **(c)**, and 10 minutes after illumination **(d)**. Scale bar: 2 μm. These indicates a p-type surface doping effect of *H*-PTCDI-C_{13} on WSe_2, which can be enhanced by light illumination and memorized through charge trapping. **(e)-(f)** Schematic band diagrams of the WSe_2/*H*-PTCDI-C_{13} interface at dark condition **(b)** and at 639 nm illumination **(c)**.

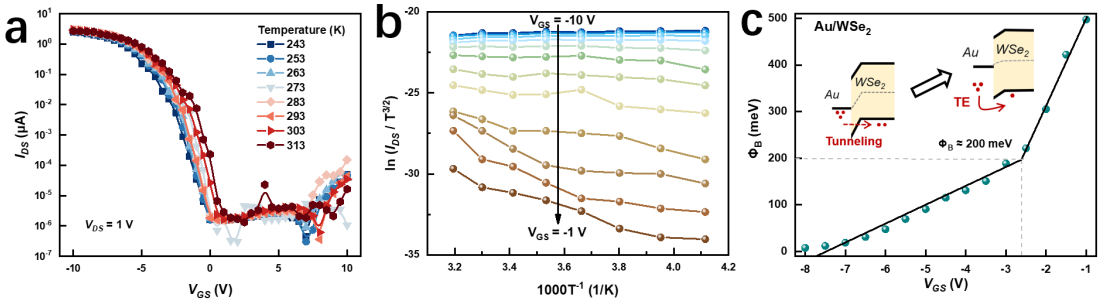

Supplementary Figure 4. Schottky barrier of Au contacted WSe_2 is calculated by 2D thermionic emission equation: $I_{DS} = \left[A^{*}T^{\frac{3}{2}}\exp\left(-\frac{q\Phi_B}{k_BT}\right)\right]\left[\exp\left(\frac{qV_{DS}}{k_BT}-1\right)\right]$. Where I_{DS} is the saturation current density, A^{*} is the effective Richardson–Boltzmann constant, T is temperature, q is the electron charge, k_B is the Boltzmann constant, and Φ_B is the Schottky barrier height. The Schottky barrier height is extracted under a flat-band gate voltage condition, which was responsible for the start of deviations from the linear behavior. **(a)** I_{DS}-V_{GS} curves of Au-WSe_2 transistor biased at 1 V with varying temperatures ranging from 313 K to 243 K. **(b)** Arrhenius plots of $ln\ (I_{DS}/T^{3/2})$ versus $1000/T$ at varying gate voltages from -10 V to -1 V of Au-WSe_2 contact. **(c)** Barrier heights of the Au-WSe_2 Schottky junctions as a function of V_{GS}. The Schottky barrier height is extracted under a flat-band voltage.

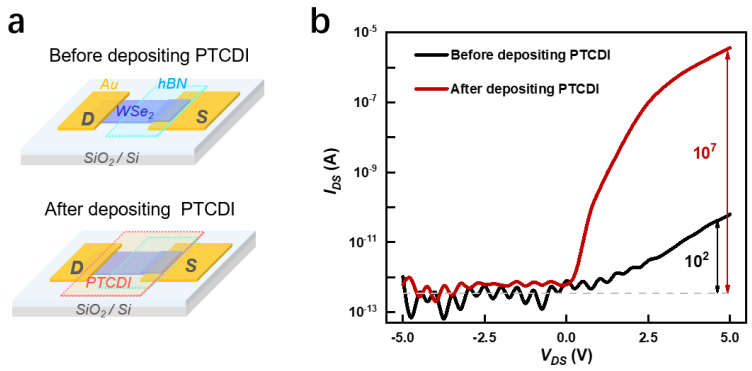

Supplementary Figure 5. **(a)-(b)** Schematic **(a)** and I_{DS}-V_{DS} curves **(b)** of an Au offset-contacted WSe_2 diode before (black curve) and after (red curve) depositing PTCDI-C_{13} layers. A rectification ratio of 10^7 is obtained after doping with PTCDI-C_{13}, which is much higher than the undoped device (~10^2).

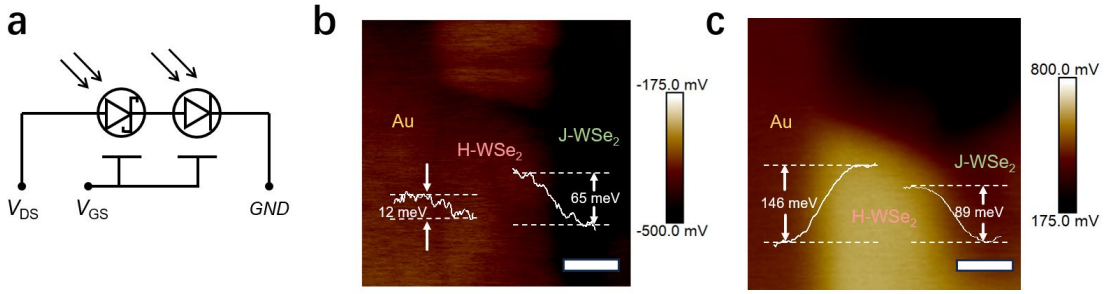

Supplementary Figure 6. **(a)** Schematic circuit diagram of the device as a series connection of a Schottky junction at the Au-WSe_2 interface and a homojunction within the doped WSe_2 channel. **(b)-(c)** Surface potential differences measured by Kelvin probe force microscopy after applying V_{GS} pulses of 15 V **(b)** and -15 V **(c)**. Scale bar: 2 μm. These measurements reveal the existence and gate tunability of both the Schottky barrier and the homojunction barrier, corresponding to the dual-junction configuration.

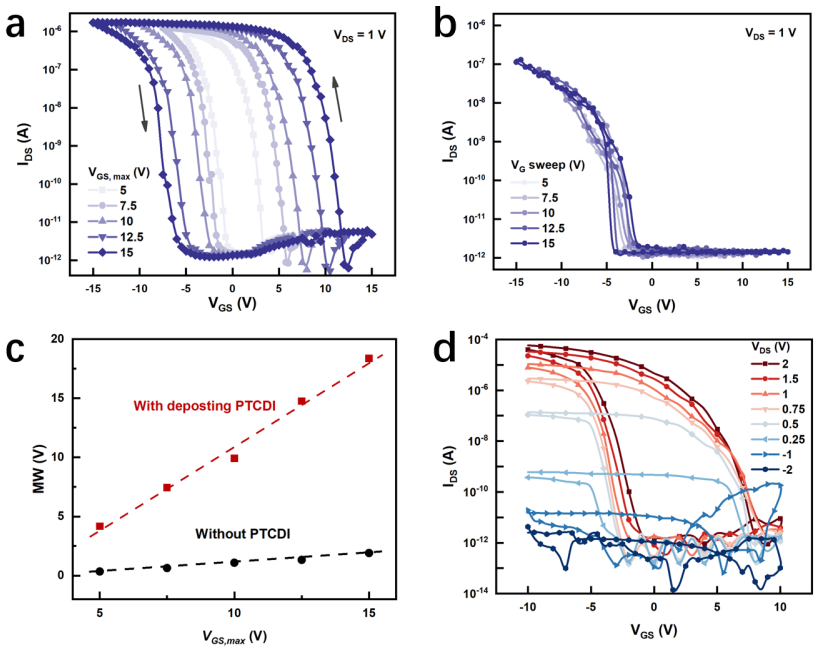

Supplementary Figure 7. **(a)-(b)** Transfer curves of the Au offset-contacted WSe_2 transistor: **(a)** after and **(b)** before the deposition of PTCDI-C_{13} layers. The curves were obtained under dual sweeping of V_{GS} ranging from ±5 to ±15 V, with a fixed bias of V_{DS} = 1 V. **(c)** Memory window width as a function of maximum V_{GS} of the device before (black dots) and after (red dots) the deposition of PTCDI-C_{13}. A significantly larger maximum width of ~18.5 V is achieved at a V_{GS} sweep of ±15 V for the PTCDI-doped device, compared to the undoped device (~1.5 V). **(d)** Transfer curves of the PTCDI-doped device under a dual sweeping of V_{GS} of ±10 V, with varying V_{DS} from -2 V to 2 V.

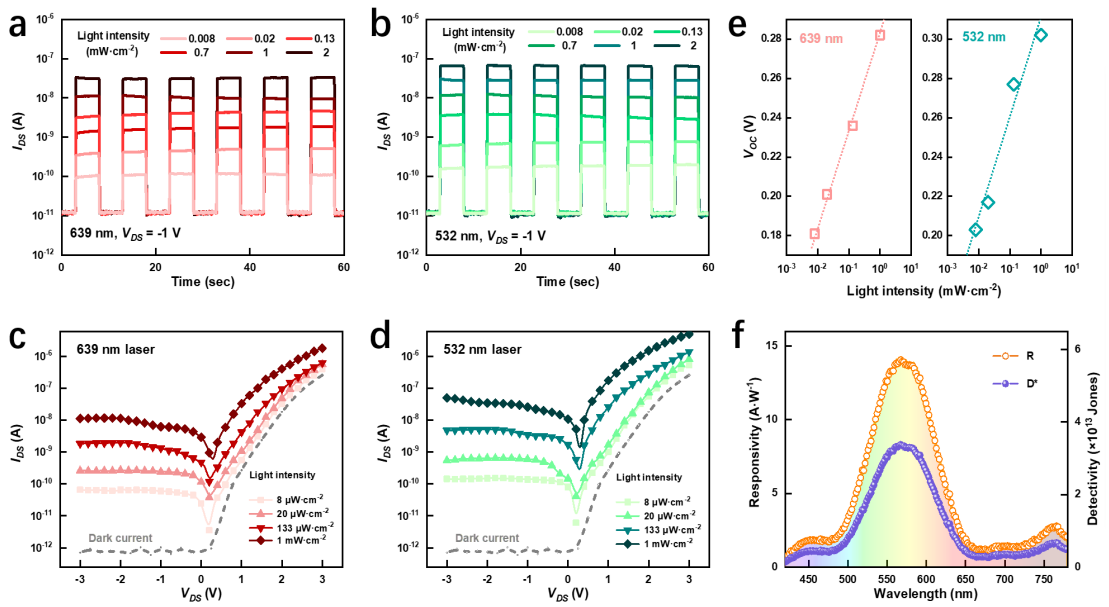

Supplementary Figure 8. **(a)-(b)** Time-resolved photocurrent curves of the PTCDI-C_{13} doped WSe_2 diode under laser illumination of 639 nm **(a)** and 532 nm **(b)** with varying light intensity ranging from 0.008 mW·cm^{-2} to 2 mW·cm^{-2}. **(c)-(d)** Photocurrent I_{DS}-V_{DS} curves of the device under laser illumination of 639 nm **(c)** and 532 nm **(d)** with varying light intensity. **(e)** Open-circuit voltage as a function of light intensity of 639 nm and 532 nm laser illuminations. **(f)** Responsivity and detectivity curves measured under light wavelength sweeping from 400 nm to 800 nm at V_{DS} = -1 V.

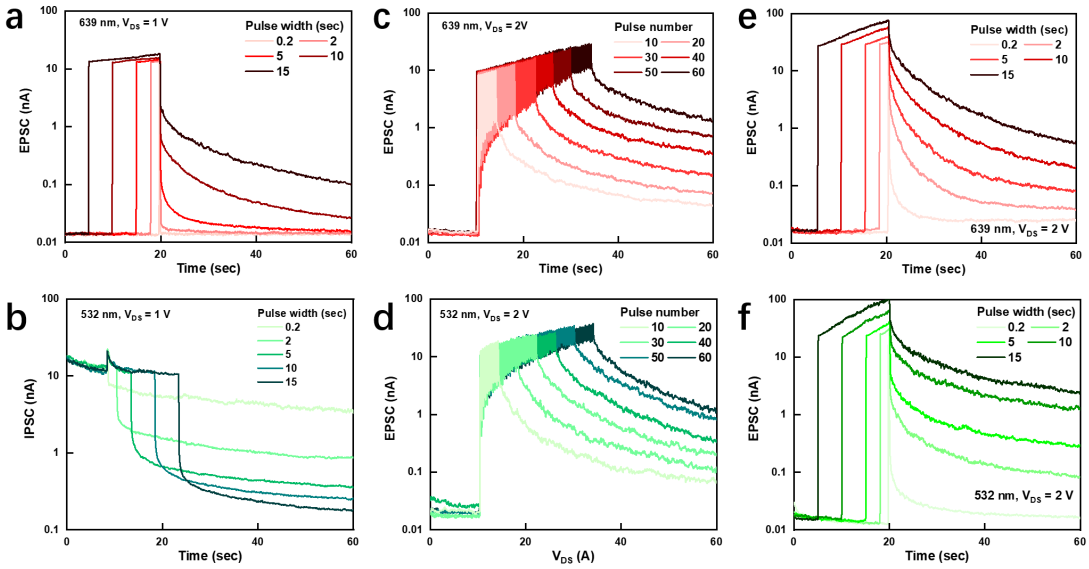

Supplementary Figure 9. **(a)-(b)** Postsynaptic current triggered by a single light pulse of varying durations from 0.2 s to 15 s at V_{DS} = 1 V under 639 nm **(a)** and 532 nm **(b)** illuminations. **(c)-(d)** Postsynaptic current triggered by continuous light pulses of varying numbers from 10 to 60 at V_{DS} = 2 V under 639 nm **(c)** and 532 nm **(d)** illuminations. **(e)-(f)** Postsynaptic current triggered by a single light pulse of varying durations from 0.2 s to 15 s at V_{DS} = 2 V under 639 nm **(e)** and 532 nm **(f)** illuminations. The light intensity is fixed at 1 mW·cm^{-2}.

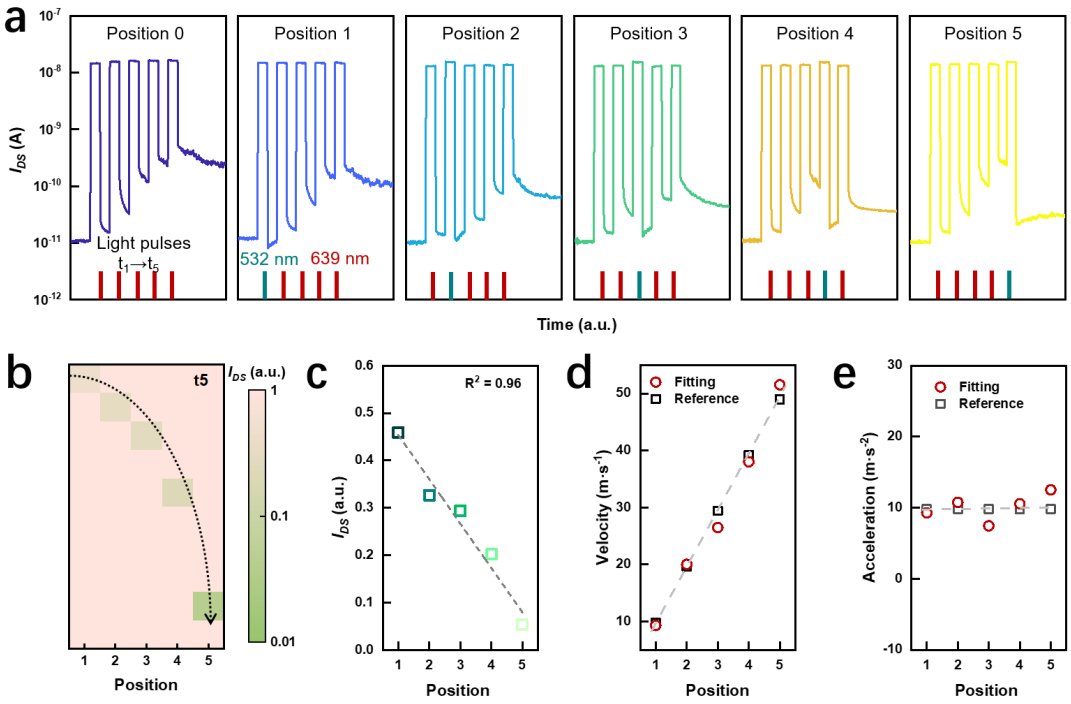

Supplementary Figure 10. **(a)** Postsynaptic current triggered by 532nm/639 nm mixed light pulses (1 mW·cm^{-2}, 5 s, 50% duty cycle) with varying sequencies. **(b)** Current mapping measured at t_5, illustrating the motion trajectory and direction of the object. **(c)** Extracted normalized current from **(b),** exhibiting an ideal linear tendency in current decay from position 1 to position 5. **(d)-(e)** Fitted velocity **(d)** and acceleration **(e)** at different potions derived from current data, corresponding to the actual motion parameters.

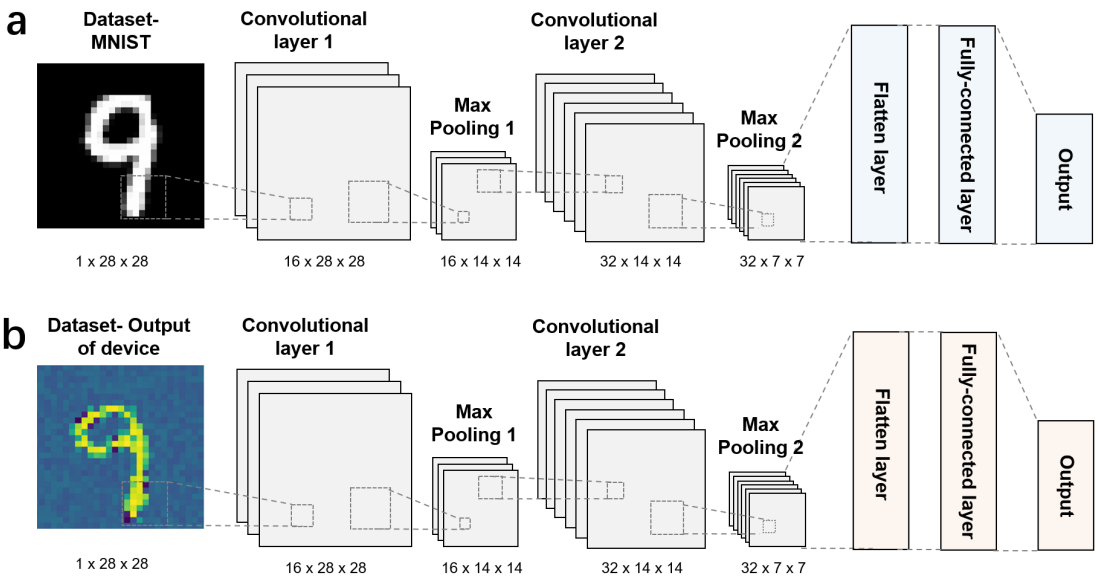

Supplementary Figure 11. **(a)-(b)** Detailed architectures of the simple convolutional neural network (CNN) for recognizing the grayscale MNIST dataset **(a)** and for interpreting device output signals into color-coded patterns **(b)**.

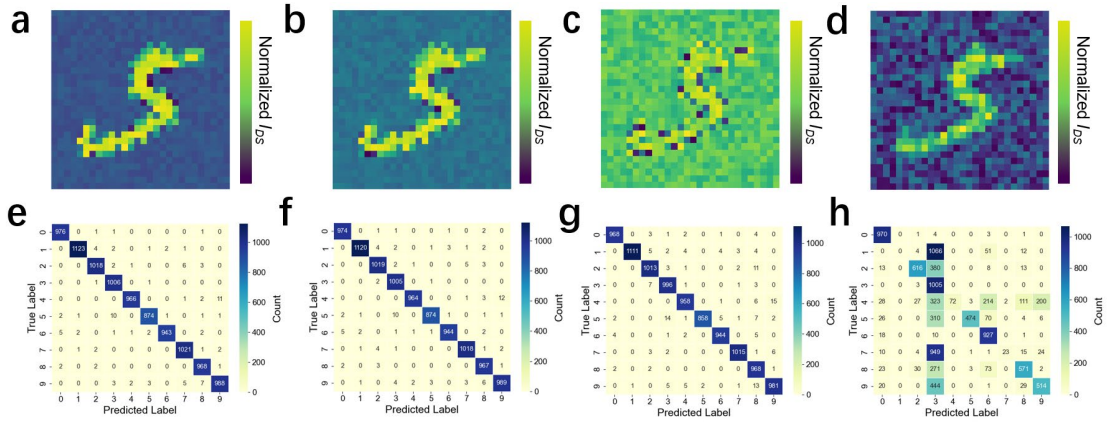

Supplementary Figure 12. Simulation result of the device in green-filter mode at V_{DS} = 1 V. **(a)-(d)** Photocurrent mapping obtained at varying decay times of 0.2 s **(a)**, 1 s **(b)**, 5 s **(c)** and 30 s **(d)**. **(e)-(h)** Corresponding confusion matrices showing a decrease in recognition accuracy of 98.99% **(e)**, 98.90% **(f)**, 98.28% **(g)** and 51.80% **(h)** at 0.2 s, 1 s, 5 s and 30 s, respectively.

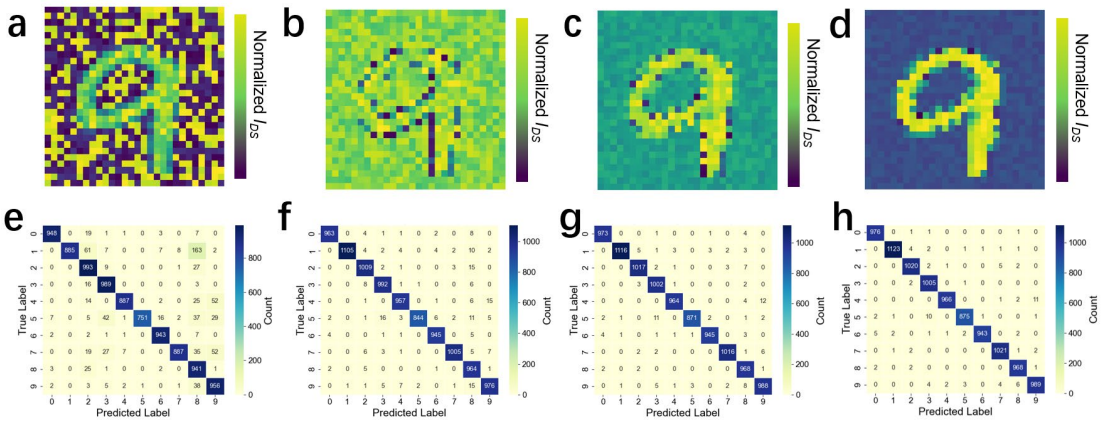

Supplementary Figure 13. Simulation result of the device in red-filter mode at V_{DS} = 2 V. **(a)-(d)** Photocurrent mapping obtained at varying decay times of 0.2 s **(a)**, 1 s **(b),** 5 s **(c)** and 30 s **(d)**. **(e)-(h)** Corresponding confusion matrices showing an increase in recognition accuracy of 91.95% **(e)**, 97.76% **(f)**, 98.76% **(g)** and 99.02% **(h)** at 0.2 s, 1 s, 5 s and 30 s, respectively.